Mon. Not. R. Astron. Soc. **358,** 1405–1416 (2005) doi:10.1111/j.1365-2966.2005.08860.x

The relationship between X-ray variability amplitude and black hole mass in active galactic nuclei

Paul M. O'Neill,[1⋆] Kirpal Nandra,[1⋆] Iossif E. Papadakis[2⋆] and T. J. Turner[3,4⋆]

[1]*Astrophysics Group, Imperial College London, Blackett Laboratory, Prince Consort Road, London SW7 2BW*
[2]*Department of Physics, University of Crete, 71 003, Heraklion, Crete, Greece*
[3]*Exploration of the Universe Division, Code 660, NASA Goddard Space Flight Center, Greenbelt, MD 20771, USA*
[4]*University of Maryland Baltimore County, 1000 Hilltop Circle, Baltimore, MD 21250, USA*

Accepted 2005 January 20. Received 2005 January 11; in original form 2004 October 19

ABSTRACT

We have investigated the relationship between the X-ray variability amplitude and black hole mass for a sample of 46 radio-quiet active galactic nuclei observed by *ASCA*. 33 of the objects in our sample exhibited significant variability over a time-scale of ∼40 ks. We determined the normalized excess variance in the 2–10 keV light curves of these objects and found a significant anticorrelation between excess variance and black hole mass. Unlike most previous studies, we have quantified the variability using nearly the same time-scale for all objects. Moreover, we provide a prescription for estimating the uncertainties in variance which accounts both for measurement uncertainties and for the stochastic nature of the variability. We also present an analytical method to predict the excess variance from a model power spectrum accounting for binning, sampling and windowing effects. Using this, we modelled the variance–mass relation assuming all objects have a universal twice-broken power spectrum, with the position of the breaks being dependent on mass. This accounts for the general form of the variance–mass relationship but is formally a poor fit and there is considerable scatter. We investigated this scatter as a function of the X-ray photon index, luminosity and Eddington ratio. After accounting for the primary dependence of excess variance on mass, we find no significant correlation with either luminosity or X-ray spectral slope. We do find an *anticorrelation* between excess variance and the Eddington ratio, although this relation might be an artefact owing to the uncertainties in the mass measurements. It remains to be established that enhanced X-ray variability is a property of objects with steep X-ray slopes or large Eddington ratios. Narrow-line Seyfert 1 galaxies, in particular, are consistent with being more variable than their broad-line counterparts solely because they tend to have smaller masses.

Key words: galaxies: active – galaxies: nuclei – galaxies: Seyfert – X-rays: galaxies.

1 INTRODUCTION

Variability was discovered in the X-ray emission from active galactic nuclei (AGN) roughly three decades ago (e.g. Marshall, Warwick & Pounds 1981, and references therein). *EXOSAT* subsequently obtained well-sampled light curves on time-scales of minutes to days, and the power spectra generated from these light curves were described as a power law $P \propto \nu^{-\alpha}$ with a steep 'red-noise' index of $\alpha \sim 1.5$ and an amplitude inversely proportional to the luminosity (Green, McHardy & Lehto 1993; Lawrence & Papadakis 1993). It was clear that this power law must break at some lower frequency, or the power would diverge, and some evidence for this was found using longer-term archival observations (McHardy 1988; Papadakis & McHardy 1995). It was not until the launch of *RXTE*, however, that this break was measured definitively (Edelson & Nandra 1999).

A number of high-quality power spectra have now been obtained, primarily using *RXTE* and *XMM–Newton* data (e.g. Uttley, McHardy & Papadakis 2002; Markowitz et al. 2003; Vaughan, Fabian & Nandra 2003b; McHardy et al. 2004). These have shown breaks to be common and emphasized the similarity of AGN power spectra to that of the black hole binary Cyg X-1. In the low/hard state, the power spectrum of Cyg X-1 exhibits a twice-broken power law which breaks from a slope of $\alpha \sim 0$ to 1 at the

⋆E-mail: p.oneill@imperial.ac.uk (PMO); k.nandra@imperial.ac.uk (KN); jhep@physics.uoc.gr (IEP); turner@lucretia.gsfc.nasa.gov (TJT)

'low-frequency break' ($\nu_{\rm LFB}$) and from $\alpha \sim 1$ to 2 at the 'high-frequency break' ($\nu_{\rm HFB}$), with $\nu_{\rm HFB} \sim$ 1–6 Hz (e.g. Belloni & Hasinger 1990b). In the high/soft state, the power spectrum exhibits only a high-frequency break, with $\nu_{\rm HFB} \sim$ 10–15 Hz (e.g. Cui et al. 1997; Revnivtsev, Gilfanov & Churazov 2000). Though still a subject of debate, the emerging consensus is that we usually see the high-frequency break in the AGN power spectra, although two breaks are apparently seen in two objects (viz. AKN 564 and NGC 3783; Papadakis et al. 2002; Markowitz et al. 2003). In another, the narrow-line Seyfert 1 (NLS1) NGC 4051, there is no low-frequency turnover to $\alpha = 0$ down to very low frequencies, which led McHardy et al. (2004) to hypothesize that this object (and possibly all NLS1s) resembled Cyg X-1 in the high/soft state.

Determining accurate power spectra for AGN is difficult, as it requires high-quality data with near-even sampling. Such data are available only for a limited number of objects and are very costly to obtain in terms of observing time. It is nonetheless very useful to quantify the X-ray variability of AGN to compare with other properties, and normalized excess variance, denoted as $\sigma^2_{\rm NXS}$, is much simpler to calculate (Nandra et al. 1997a). An anticorrelation was found between excess variance and luminosity for a sample of AGN observed by the *Advanced Satellite for Cosmology and Astrophysics* (*ASCA*), confirming the *EXOSAT* results but with a larger sample of objects (Nandra et al. 1997a). Later work also using *ASCA* data revealed that, for a given luminosity, the X-ray light curves of NLS1s exhibit a larger excess variance than the classical Seyfert 1 galaxies (Leighly 1999a; Turner et al. 1999).

Lu & Yu (2001) and Bian & Zhao (2003), again using *ASCA* data, studied the relationship between the excess variance (on a time-scale of roughly 1 d) and the black hole mass. Those studies revealed an anticorrelation between $\sigma^2_{\rm NXS}$ and mass, which is suggestive that this is the primary relationship rather than with luminosity. The NLS1s appeared to follow the same relationship as the other AGN.

Papadakis (2004) investigated the relationship between excess variance and black hole mass on much longer time-scales (∼300 d) using *RXTE* data on a sample of 10 AGN. The classical Seyfert 1 galaxies followed a variance–mass relation that is consistent with a universal power-spectral shape as described above for the low/hard state of Cyg X-1. In the universal model used by Papadakis (2004), $\nu_{\rm HFB}$ is inversely proportional to black hole mass, and the amplitude, when represented in power × frequency space, is assumed to be constant. In agreement with the power spectrum analysis of McHardy et al. (2004), Papadakis (2004) found that the NLS1 NGC 4051 did not follow the same variance–mass relationship described by the classical Seyfert 1s. The excess variance of NGC 4051 was consistent with a singly broken power law, breaking from $\alpha = 1$ to 2, with a break frequency 20 times higher than that deduced for the other Seyfert 1s.

These works show that excess variance can be a useful complement to full-blown power-spectral analysis, and have the advantage that they can be applied to a larger number, and wider variety of objects. As has been shown by Vaughan et al. (2003a), some caution must be exercised when interpreting excess variance measurements, primarily due to the red-noise shape of the power spectra and the stochastic nature of the variability. Such effects have not been accounted for in the majority of previous works. The intention of the work presented here is to investigate the relationship between excess variance and mass in a large sample of AGN, improving on these previous studies by fully accounting for measurement uncertainties, sampling and red-noise effects in the calculation of the excess variance and its uncertainty.

2 THE TARTARUS DATA BASE AND THE AGN SAMPLE

The Tartarus[1] data base contains products for *ASCA* observations with targets designated as AGN (Turner et al. 2001). We selected radio-quiet objects that have data in the Tartarus (Version 3.0) data base and also for which we could conveniently obtain a measurement of the black hole mass, $M_\bullet$. Seyfert 2 objects were excluded from our sample, with the exception of NGC 5506 because for this object we are confident of seeing the X-ray emission directly (Blanco, Ward & Wright 1990). This initial sample comprised 68 AGN. We utilized the Tartarus analysis pipeline to extract light curves for the objects in this sample. As we describe in detail in the following section, not all light curves were suitable for our analysis. Having screened the available data, there remained 46 objects for which we could suitably characterize the X-ray variability. These objects are listed in Table 1. Note that, while a flux limit was not formally applied to our sample, the effect of the screening process was to exclude objects having a low counting rate.

Recent progress in measuring black hole masses has made possible the work we present here. We preferentially used the reverberation-mapping mass estimate from Peterson et al. (2004). If this was not available then we used the mass estimate as determined from either the stellar velocity dispersion (Gebhardt et al. 2000) or the empirical relationship between the broad-line region radius and 5100-Å luminosity (Wandel, Peterson & Malkan 1999). The masses are given in Table 1 where we also list the method used to determine the mass and the corresponding reference. The masses for most objects were available in the literature. For eight objects in Table 1 we obtained optical spectral information from Grupe et al. (2004) and utilized equation (6) from Kaspi et al. (2000) and equations (1) and (2) from Woo & Urry (2002) to determine $M_\bullet$.

The 2–10 keV luminosity $L_{2-10\,\rm keV}$ and hard-X-ray (either 2–10 keV or 3–10 keV) photon index Γ are also listed in Table 1 for those objects in which we detected variability. The majority of $L_{2-10\,\rm keV}$ and Γ values were taken from Nandra & Pounds (1994), Nandra et al. (1997b), Reynolds (1997), Leighly (1999b), George et al. (2000), Iwasawa et al. (2000) and Reeves & Turner (2000). For the objects PG 0026+129, NGC 985, F 303 and MRK 279, we fitted the available *ASCA* data to obtain $L_{2-10\,\rm keV}$ and Γ. The SIS0, SIS1, GIS2 and GIS3 spectra were fitted simultaneously in the 2–10 keV rest-frame energy range. We used an absorbed power law, with $N_{\rm H}$ constrained to be greater than the galactic value which we obtained using the NASA HEASARC 'nH' tool.[2] For our luminosity calculations we obtained redshifts from the NASA/IPAC Extragalactic Data base[3] and used $H_0 = 75$ km s^{-1} and $q_0 = 0.5$. All $L_{2-10\,\rm keV}$ values collected from the literature were transformed to this cosmology as required.

3 EXCESS VARIANCE ANALYSIS

The number of *ASCA* observing sequences available for each object is shown in Table 1. We extracted a 2–10 keV combined SIS0+SIS1+GIS2+GIS3 light curve from each sequence. These initial light curves had a resolution of 16 s and each bin was required to be fully exposed. The light curves were then rebinned to a resolution of 256 s.

[1] http://astro.imperial.ac.uk/Research/Tartarus
[2] http://heasarc.gsfc.nasa.gov/cgi-bin/Tools/w3nh/w3nh.pl
[3] http://nedwww.ipac.caltech.edu/

Table 1. X-ray spectral and variability information for objects having at least one valid light-curve segment. The 2–10 keV luminosity and hard-X-ray photon index are given for objects in which variability was detected.

Name	$M_\bullet$	L_X	Γ	Num. Seq.	Num. Seg.	σ^2_{NXS} ± Boot. Unc.	log σ^2_{NXS} ± Total Unc.	Δ log σ^2_{NXS} ± Total Unc.	Refs.
(1)	(2)	(3)	(4)	(5)	(6)	(7)	(8)	(9)	(10)
MRK 335	7.15	43.07	1.87	1	1	$(3.12 \pm 1.87) \times 10^{-3}$	-2.51 ± 0.41	-0.44 ± 0.41	R,1,2
PG 0026+129	8.59	44.53	1.96	1	3	$(1.31 \pm 1.92) \times 10^{-3}$	-2.88 ± 0.66	0.61 ± 0.66	R,1
TON S180	7.09	43.58	2.43	2	26	$(1.59 \pm 0.10) \times 10^{-2}$	-1.80 ± 0.07	0.21 ± 0.07	L,3,4
I Zw 1	7.20	43.35	2.40	1	1	$(1.88 \pm 0.92) \times 10^{-2}$	-1.73 ± 0.39	0.39 ± 0.39	L,3,4
F 9	8.41	43.91	1.91	8	6	$(3.49 \pm 5.52) \times 10^{-4}$	-3.46 ± 0.70	-0.16 ± 0.70	R,1,2
RX J0152.4−2319	7.87	...	...	1	2	$<6.5 \times 10^{-3}$	<-1.94	...	L,5
MRK 0586	7.86	44.07	2.22	1	3	$(2.57 \pm 0.75) \times 10^{-2}$	-1.59 ± 0.22	1.17 ± 0.22	L,6,4
MRK 1040	7.64	42.40	1.69	1	1	$(1.20 \pm 0.65) \times 10^{-2}$	-1.92 ± 0.40	0.62 ± 0.40	S,6,7
NGC 985	8.05	43.50	1.73	1	2	$(3.47 \pm 1.76) \times 10^{-3}$	-2.46 ± 0.32	0.48 ± 0.32	L,5
1H 0419−577	8.58	...	...	2	3	$<4.31 \times 10^{-3}$	< -2.12	...	L,3
F 303	6.37	43.03	1.92	1	1	$(6.72 \pm 6.03) \times 10^{-3}$	-2.17 ± 0.44	-0.74 ± 0.44	L,5
AKN 120	8.18	43.88	1.93	1	2	$(3.78 \pm 7.67) \times 10^{-4}$	-3.42 ± 0.91	-0.35 ± 0.91	R,1,8
PG 0804+761	8.84	...	...	1	2	$<3.37 \times 10^{-3}$	< -2.23	...	R,1
PG 0844+349	7.97	...	...	1	2	$<1.17 \times 10^{-2}$	< -1.69	...	R,1
MRK 110	7.40	...	...	1	1	$< 1.63 \times 10^{-3}$	< -2.55	...	R,1
PG 0953+415	8.44	...	...	1	2	$<8.18 \times 10^{-3}$	< -1.85	...	R,1
NGC 3227	7.63	41.66	1.52	2	4	$(2.41 \pm 0.20) \times 10^{-2}$	-1.62 ± 0.16	0.91 ± 0.16	R,1,2
MRK 142	6.76	43.17	2.12	2	1	$(4.54 \pm 1.33) \times 10^{-2}$	-1.34 ± 0.34	0.37 ± 0.34	L,5,4
HE 1029−1401	9.08	44.44	1.83	1	2	$(1.02 \pm 1.21) \times 10^{-3}$	-2.99 ± 0.56	0.98 ± 0.56	L,6,9
NGC 3516	7.63	43.08	1.83	5	18	$(3.70 \pm 0.45) \times 10^{-3}$	-2.43 ± 0.10	0.10 ± 0.10	R,1,2
PG 1116+215	8.21	...	...	1	1	$<1.06 \times 10^{-2}$	< -1.73	...	L,6
EXO 1128.1+6908	7.02	...	...	1	1	$<1.78 \times 10^{-2}$	<-1.51	...	L,5
NGC 3783	7.47	42.90	1.70	9	8	$(3.91 \pm 0.51) \times 10^{-3}$	-2.41 ± 0.13	-0.03 ± 0.13	R,1,2
NGC 4051	6.28	41.21	1.92	2	6	$(8.62 \pm 0.66) \times 10^{-2}$	-1.06 ± 0.09	0.31 ± 0.09	R,1,2
NGC 4151	7.12	42.62	1.53	13	29	$(2.79 \pm 0.22) \times 10^{-3}$	-2.55 ± 0.07	-0.51 ± 0.07	R,1,2
PG 1211+143	8.16	...	...	1	1	$<2.39 \times 10^{-2}$	< -1.38	...	R,1
MRK 766	6.54	42.73	2.16	1	2	$(4.02 \pm 0.48) \times 10^{-2}$	-1.40 ± 0.16	0.15 ± 0.16	L,6,2
NGC 4395	4.11	39.99	1.7	5	6	$(1.13 \pm 0.14) \times 10^{-1}$	-0.95 ± 0.10	0.17 ± 0.10	L,10,11
NGC 4593	6.73	42.98	1.81	2	1	$(1.42 \pm 0.21) \times 10^{-2}$	-1.85 ± 0.33	-0.16 ± 0.33	R,1,8
WAS 61	6.66	...	...	1	1	$<6.95 \times 10^{-3}$	< -1.92	...	L,5
PG 1244+026	6.07	43.03	2.46	1	2	$(2.60 \pm 0.62) \times 10^{-2}$	-1.59 ± 0.18	-0.31 ± 0.18	L,5,12
MCG−6-30-15	6.19	42.72	2.00	6	48	$(4.16 \pm 0.13) \times 10^{-2}$	-1.38 ± 0.03	-0.05 ± 0.03	L,3,2
IC 4329A	7.00	43.59	1.71	5	6	$(2.36 \pm 2.44) \times 10^{-4}$	-3.63 ± 0.47	-1.70 ± 0.47	R,1,2
MRK 279	7.54	43.66	1.99	1	1	$(2.32 \pm 0.84) \times 10^{-3}$	-2.63 ± 0.36	-0.19 ± 0.36	R,1
NGC 5506	7.94	42.73	2.08	1	2	$(1.06 \pm 0.14) \times 10^{-2}$	-1.97 ± 0.23	0.87 ± 0.23	S,13,8
NGC 5548	7.83	43.41	1.79	11	16	$(9.42 \pm 2.67) \times 10^{-4}$	-3.03 ± 0.14	-0.30 ± 0.14	R,1,2
MRK 1383	9.11	...	...	1	1	$< 6.33 \times 10^{-3}$	< -1.96	...	R,1
MRK 478	7.34	43.50	2.06	1	2	$(6.14 \pm 3.75) \times 10^{-3}$	-2.21 ± 0.35	0.04 ± 0.35	L,3,4
MRK 841	8.10	43.54	2.00	3	5	$(1.14 \pm 0.93) \times 10^{-3}$	-2.94 ± 0.38	0.05 ± 0.38	L,6,2
MRK 290	7.05	43.22	1.77	1	2	$(4.11 \pm 2.15) \times 10^{-3}$	-2.39 ± 0.32	-0.41 ± 0.32	L,3,7
IRAS 17020+4544	6.77	43.73	2.37	1	2	$(5.47 \pm 2.00) \times 10^{-3}$	-2.26 ± 0.28	-0.54 ± 0.28	L,14,4
MRK 509	8.16	44.03	1.82	11	2	$(5.75 \pm 7.17) \times 10^{-4}$	-3.24 ± 0.59	-0.19 ± 0.59	R,1,2
AKN 564	6.06	43.38	2.58	13	70	$(5.34 \pm 0.14) \times 10^{-2}$	-1.27 ± 0.03	0.00 ± 0.03	L,3,4
RX J2248.6−5109	7.67	...	...	1	1	$<1.08 \times 10^{-2}$	<-1.73	...	L,5
NGC 7469	7.09	43.25	1.84	3	2	$(4.68 \pm 1.60) \times 10^{-3}$	-2.33 ± 0.27	-0.32 ± 0.27	R,1,2
MCG−2-58-22	8.54	...	...	2	4	$<1.53 \times 10^{-3}$	<-2.58	...	L,3

The objects are listed in order of RA. (1) Object name. (2) Log of black hole mass in units of $M_\odot$. (3) Log of 2–10 keV luminosity in units of erg s^{-1}. (4) Hard-X-ray photon index. (5) Number of available *ASCA* observing sequences. (6) Number of usable light-curve segments. (7) Mean normalized excess variance with the uncertainty or upper limit as determined from the bootstrap simulations. (8) Log of the mean normalized excess variance with the uncertainty as determined by combining the bootstrap uncertainty and the derived red-noise scatter. (9) Residuals from the best-fitting universal model with the uncertainty as determined by combining the bootstrap uncertainty and the derived red-noise scatter. (10) Method used to determine the black hole mass and references for the mass and X-ray spectral properties. The methods, in order of preference, are as follows: R, reverberation mapping; S, stellar velocity dispersion; L, relationship between broad-line region radius and optical luminosity. References: 1, Peterson et al. (2004); 2, Nandra et al. (1997b); 3, Bian & Zhao (2003); 4, Leighly (1999b); 5, Grupe et al. (2004); 6, Woo & Urry (2002); 7, Reynolds (1997); 8, Nandra & Pounds (1994); 9, Reeves & Turner (2000); 10, Filippenko & Ho (2003); 11, Iwasawa et al. (2000); 12, George et al. (2000); 13, Papadakis (2004); 14, Wang & Lu (2001). The reference for the black hole mass of each object is listed first.

3.1 Excess variance calculation

For a red-noise process, the variance in a light curve depends both on the power spectrum of the variations and also on the time resolution and duration of the light curve. This means that different σ^2_{NXS} measurements are only strictly comparable if the durations of the light curves are equal. Therefore, we subdivided the light curve from each sequence into many segments of similar duration. The

advantage of using long durations is that the amplitude of variability increases, and the number of points used to calculate $\sigma^2_{\rm NXS}$ is also larger, reducing the measurement uncertainty. On the other hand, using short durations has the advantage that more light-curve segments can be included. We chose a nominal segment length of 40 ks for our analysis as a trade-off between these considerations. In reality we chose a duration of 39 936 ks which is an integer multiple of our 256-s time bin.

The subdividing of the light curves proceeded as follows. First, the earliest 40-ks segment of the light curve for a certain observing sequence was selected. Then, beginning with the next exposed bin following the end of this first segment, another 40-ks segment was selected. This continued until the light curve had been completely subdivided. Note that the actual duration of these light curves, which we define as the time between the first and last exposed bin, can be less than 40 ks because the dividing point between segments can occur when there is a gap in the data train. We accepted all resulting light-curve segments that had a duration >30 ks.

To ensure Gaussian statistics, we required each 256-s bin to contain at least 20 counts. The number of counts in a certain 256-s bin depends both on the source counting rate and the fractional exposure of that bin. We do not wish to reject entire observing sequences simply because some of the bins have a low exposure, but those in which fully exposed bins have <20 counts should be excluded. If we were to remove bins simply because they had a low counting rate, we would be biased against observing objects when their intensity is low. Selecting according to fractional exposure, on the other hand, can remove bins having too few counts without introducing this bias, as fractional exposure is not related to the intensity of the source. If, for example, there are fully exposed bins with <20 counts, the entire sequence was discarded. This is the case when we are dealing with a weak source. For brighter sources where only underexposed bins have <20 counts, we excise all bins below some minimal fractional exposure. This gets rid of the non-Gaussian bins, allowing us to keep the remainder of the light curve for further analysis, but introduces no bias against those times when the source is weak due to true flux variability.

Finally, we further required the truncated and screened light-curve segments to have at least 20 bins, so that the variance could be determined accurately.

This procedure resulted in 46 objects having at least one valid light-curve segment, and a total of 305 valid segments in all. The number of segments for each object is given in Table 1. The mean durations of the light-curve segments for each object were in the range 35–40 ks in the observers frame. The 48 objects in our sample have redshifts in the range 0.001–0.234. Taking into account the redshift of each object, the rest-frame mean durations were in the range 30–40 ks. We expect the effect of these slightly different durations to be small. For a power spectrum with a power-law slope of $\alpha = 2$, the worst case we expect, a ∼25 per cent reduction in the light-curve duration (i.e. from 40 to 30 ks), results in a reduction in the $\sigma^2_{\rm NXS}$ of only ∼0.1 dex. As presented later in this section, the uncertainties in most of our observed $\sigma^2_{\rm NXS}$ values are a few to several times larger than 0.1 dex. Therefore, the ∼25 per cent difference between the shortest and longest mean light-curve duration can be neglected and allows us to use more data than would have been available if we had imposed a strict limit on duration.

We tested to see which objects exhibited significant variability by performing a chi-squared test. The χ^2 corresponding to the hypothesis of a constant counting rate was determined for each ∼40-ks light-curve segment. Then, for each object, we summed all of the χ^2s and degrees of freedom (DOFs) to test whether that object is variable. We detected variability in 33 objects at the 95 per cent confidence level. We then calculated the excess variance in each light-curve segment with the following expression:

$$\sigma^2_{\rm NXS} = \frac{1}{N\mu^2}\sum_{i=1}^{N}\left[(X_i-\mu)^2-\sigma_i^2\right] \quad (1)$$

where N is the number of bins in the segment, X_i and σ_i are the counting rates and uncertainties, respectively, in each bin, and μ is the unweighted arithmetic mean of the counting rates. For objects with more than one valid segment, the unweighted average excess variance was determined. A major advantage of our work is that, given the large number of light curves available, there is often more than one valid segment per object (see Table 1). Taking the mean $\sigma^2_{\rm NXS}$ of these multiple segments reduces the potentially large uncertainty owing to the stochastic nature of the variability (see below). When calculating the mean excess variance we used *all* valid light-curve segments for a particular object, including those segments that did not, in themselves, exhibit variability based on the χ^2 test.

3.2 Estimating the uncertainties in $\sigma^2_{\rm NXS}$

Estimating the uncertainty for excess variance is somewhat complicated. Analytical prescriptions have been given in the literature by Nandra et al. (1997a; their correct formula is given by Turner et al. 1999), Edelson et al. (2002) and Vaughan et al. (2003a). The last authors also discussed the uncertainties in $\sigma^2_{\rm NXS}$ on the basis of simulated red-noise light curves. These uncertainties depend both on measurement uncertainties (e.g. Poisson noise) in the light-curve data, and the stochastic nature of the variability: any given light-curve segment represents just one realization of a random process, and thus can exhibit a different mean and variance from the true value, or another random segment. This 'noise' uncertainty can be very large, especially for a single realization. One must, therefore, account for this uncertainty before apparent differences in $\sigma^2_{\rm NXS}$, either in a given source (Nandra & Papadakis 2001) or in comparing sources (e.g. Turner et al. 1999), can be considered robust. The measurement and noise uncertainties on $\sigma^2_{\rm NXS}$ are unrelated, so can and must be estimated separately.

To estimate the uncertainty in $\sigma^2_{\rm NXS}$ owing to measurement uncertainties, we used bootstrap simulations (the reader is directed to Press et al. 2001, for a discussion on bootstrap simulations). Suppose that the observed light curve contains N bins. This light curve is a distribution of N counting rates and corresponding Poisson-noise uncertainties from which we calculate $\sigma^2_{\rm NXS}$. Note that calculating $\sigma^2_{\rm NXS}$ does not depend on the bins being in time order. A bootstrap simulation involves randomly selecting, from that distribution, a new set of N bins. The duplication of bins is permitted during the selection process. This, then, results in the creation of a slightly different distribution of counting rates, and $\sigma^2_{\rm NXS}$ can be determined for this new distribution. If one repeats the entire process many times, the resulting distribution of simulated $\sigma^2_{\rm NXS}$ values provides an estimate of the uncertainty in $\sigma^2_{\rm NXS}$.

We performed a series of 10 000 bootstrap simulations to determine the uncertainty in the *mean* observed $\sigma^2_{\rm NXS}$ for each object in our sample. Each of these simulations involved: simulating a new 'light curve' from each valid light-curve segment, determining $\sigma^2_{\rm NXS}$ for those simulated light curves, and then determining the mean of these simulated $\sigma^2_{\rm NXS}$ values. We were thus able to generate 10 000 simulated values of the mean $\sigma^2_{\rm NXS}$. The standard deviation of these values was taken to be the measurement uncertainty in the mean

observed $\sigma^2_{\rm NXS}$. We refer to this value as the 'bootstrap uncertainty' and denote it as $\Delta_{\rm boot}(\sigma^2_{\rm NXS})$.

Estimates of the uncertainty owing to the noise process have been presented by Vaughan et al. (2003a), based on light-curve simulations, who showed that the noise uncertainty is proportional to the mean value of the variance. The constant of proportionality depends on the power-spectrum shape, which we do not know a priori. Therefore, as pointed out by Vaughan et al. (2003a), it is preferable to determine the uncertainties in $\sigma^2_{\rm NXS}$ directly from the data.

Our large data base contains six objects (viz. AKN 564, MCG−6-30-15, TON S180, NGC 4151, 3516 and 5548) with a sufficient number of light-curve segments (>15) to make a meaningful estimate of the fractional uncertainty in $\sigma^2_{\rm NXS}$ owing to the noise nature of our light curves. First, we determined the standard deviation $\sigma_{\rm obs}$ of the observed $\sigma^2_{\rm NXS}$ values for each object. We then determined, from the bootstrap uncertainty, the standard deviation $\sigma_{\rm meas}$ that we would expect to observe in the distribution of the $\sigma^2_{\rm NXS}$ values if the scatter was owing only to measurement uncertainties. We subtracted $\sigma_{\rm meas}$ from $\sigma_{\rm obs}$, in quadrature, to obtain the standard deviation $\sigma_{\rm noise}$ in the observed $\sigma^2_{\rm NXS}$ values that is owing only to the stochastic nature of the variability. We then determined, for each of the six distributions, the ratio between $\sigma_{\rm noise}$ and mean $\sigma^2_{\rm NXS}$. We shall refer to this ratio as the 'fractional standard deviation' and denote it as $\sigma_{\rm frac}$. The fractional standard deviations for the six objects were: 0.49 (AKN 564), 0.47 (MCG−6-30-15), 0.69 (TON S180), 0.79 (NGC 4151), 0.82 (NGC 3516) and 0.61 (NGC 5548). These values of $\sigma_{\rm frac}$ show that, *even in the absence of measurement uncertainties*, one can expect noise uncertainties in the range ∼50–80 per cent for individual measurements of $\sigma^2_{\rm NXS}$ (see also Vaughan et al. 2003a). This highlights the need for obtaining many realizations (i.e. many measurements of $\sigma^2_{\rm NXS}$), regardless of the level of Poisson noise in the data.

Vaughan et al. (2003a) showed that the uncertainty in the estimated variance of a red-noise light curve increases with the steepness of the power spectrum slope. Power-spectral analyses of AGN have revealed that the value of $\nu_{\rm HFB}$ generally decreases with increasing black hole mass. This means that the shape of the power spectrum in the frequency range probed by our light curves (∼2.5×10^{-5} to 4×10^{-3} Hz) is expected to vary as a function of $M_\bullet$, such that the objects with the highest $M_\bullet$ should exhibit the steepest ($\alpha \sim 2$) power spectra. We expect, then, that the scatter in $\sigma^2_{\rm NXS}$ owing to red-noise fluctuations should also increase with mass. The lowest-mass objects are AKN 564 and MCG−6-30-15, and the observed values of $\nu_{\rm HFB}$ for these fall within the frequency range of our data (Papadakis et al. 2002; Vaughan et al. 2003b). We therefore expect $\sigma_{\rm frac}$ for this pair of objects to be less than the others. This does indeed appear to be the case: the $\sigma_{\rm frac}$ values of AKN 564 and MCG−6-30-15 are both less than those of TON S180, NGC 4151, 3516 and 5548. However, we possess only a limited number of individual $\sigma^2_{\rm NXS}$ measurements to estimate both the mean and standard deviation of each distribution, so it is possible that this apparent difference is not statistically significant. We decided, therefore, to compare the six distributions of $\sigma^2_{\rm NXS}$ values using a series of Kolmogorov–Smirnov (K–S) tests. Before we could compare the distributions, we first had to correct each of them for the effect of measurement uncertainties. To do this, we scaled the deviations of the observed $\sigma^2_{\rm NXS}$ values so that the standard deviation of the 'corrected' distribution was equal to $\sigma_{\rm noise}$, with the mean $\sigma^2_{\rm NXS}$ remaining unchanged. We then normalized each of the corrected distributions by dividing the $\sigma^2_{\rm NXS}$ values by the mean. The corrected and normalized $\sigma^2_{\rm NXS}$ distributions for AKN 564 and MCG−6-30-15 are consistent with being drawn from the same distribution. The same

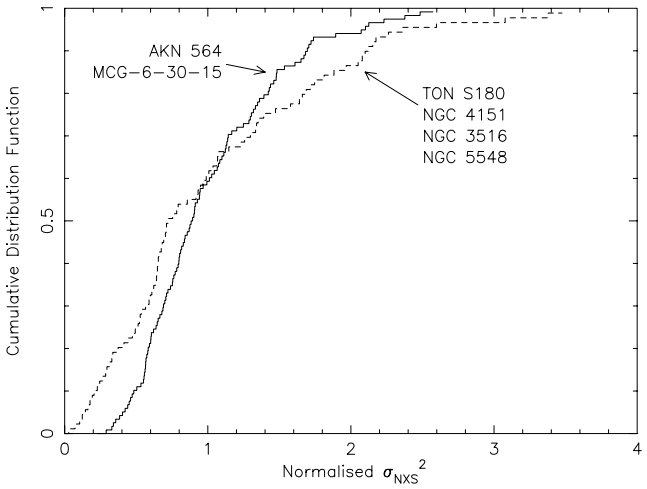

Figure 1. Cumulative distribution functions of the combined normalized $\sigma^2_{\rm NXS}$ distributions of AKN 564 and MCG−6-30-15 (solid line) and TON S180, NGC 4151, 3516 and 5548 (dashed line).

is true when comparing the other four distributions with each other. We then created two, combined distributions: one for AKN 564 and MCG−6-30-15; and another for TON S180, NGC 4151, 3516 and 5548. The fractional standard deviations from these two combined distributions were 0.48 (AKN 564, MCG−6-30-15) and 0.74 (TON S180, NGC 4151, 3516, 5548), and a K–S test showed them to be different at the 95 per cent confidence level. The cumulative distribution functions of the combined distributions are presented in Fig. 1. Combining the normalized, corrected distributions of all six objects resulted in a $\sigma_{\rm frac}$ of 0.61.

For the objects AKN 564, MCG−6-30-15, TON S180, NGC 4151, 3516 and 5548, we determined the total uncertainty $[\Delta_{\rm tot}(\sigma^2_{\rm NXS})]$ in the mean excess variance directly from their respective values of $\sigma_{\rm obs}$. For each of the other objects, we estimated the noise uncertainty and combined it in quadrature with the bootstrap uncertainty $[\Delta_{\rm boot}(\sigma^2_{\rm NXS})]$ using the following expression:

$$\Delta_{\rm tot}\left(\sigma^2_{\rm NXS}\right) = \sqrt{\left(\frac{\sigma_{\rm frac}\sigma^2_{\rm NXS}}{\sqrt{N_{\rm seg}}}\right)^2 + \left[\Delta_{\rm boot}\left(\sigma^2_{\rm NXS}\right)\right]^2} \qquad (2)$$

where $\sigma^2_{\rm NXS}$ is the mean excess variance and $N_{\rm seg}$ is the number of available light-curve segments. For objects with $\log M_\bullet > 6.54$ we adopted a fractional standard deviation of $\sigma_{\rm frac} = 0.74$, while for the objects with $\log M_\bullet \leqslant 6.54$ we adopted a value of $\sigma_{\rm frac} = 0.48$. These ranges in mass were selected on the basis that the object MRK 766, which has $\log M_\bullet = 6.54$, is the most massive object that has an observed $\nu_{\rm HFB}$ in the frequency range probed by our ∼40-ks light curves (e.g. Papadakis et al. 2002; Vaughan & Fabian 2003; Marshall et al. 2004; Vaughan et al. 2005, and see Introduction). For objects more massive than this we expect $\nu_{\rm HFB}$ to be less than our observed frequency range. In the absence of a measurement of $M_\bullet$ or any information regarding the shape of the power spectrum, the mean value of $\sigma_{\rm frac} = 0.61$ can be adopted.

The $\sigma^2_{\rm NXS}$ upper limits for the non-variable objects were also estimated by combining the two components of uncertainty. We multiplied the 1σ bootstrap uncertainty by the appropriate fractional standard deviation of the noise uncertainty. This value was then multiplied by 3 to provide an estimate of the 3σ upper limit. We also estimated the 3σ 'bootstrap upper limit' by multiplying the bootstrap uncertainty $\Delta_{\rm boot}(\sigma^2_{\rm NXS})$ by 3.

The distributions of the $\sigma^2_{\rm NXS}$ values for AKN 564 and MCG−6-30-15 are quite asymmetric, with each having an extended tail towards high values of $\sigma^2_{\rm NXS}$. However, the distributions of $\log \sigma^2_{\rm NXS}$ look much more symmetric. This is not surprising as it is well known that the logarithmic transformation of a random variable with an extended tail in its distribution brings that distribution much closer to 'normality' (e.g. Papadakis & Lawrence 1993). Ideally, then, we would like to estimate $\log \sigma^2_{\rm NXS}$ from each segment and then determine the mean of $\log \sigma^2_{\rm NXS}$ for each object. Unfortunately, we cannot use this method because $\sigma^2_{\rm NXS}$ is negative for some light-curve segments. We did, however, determine the logarithm of the mean $\sigma^2_{\rm NXS}$, which brings the distribution of the mean $\sigma^2_{\rm NXS}$ closer to normality. We also transformed the uncertainties $\Delta_{\rm tot}(\sigma^2_{\rm NXS})$ to be the uncertainty in the logarithm of the mean $\sigma^2_{\rm NXS}$.

The mean $\sigma^2_{\rm NXS}$ values, uncertainties and upper limits are listed in Table 1. The column listing $\sigma^2_{\rm NXS}$ gives the uncertainty and 3σ upper limit as determined from only the bootstrap simulations. The uncertainties and upper limits given in the column with $\log \sigma^2_{\rm NXS}$ include also the noise uncertainty.

3.3 The variance–mass relation

The relationship between $\log \sigma^2_{\rm NXS}$ and $\log M_\bullet$ is presented in Fig. 2. It is clear that there is a strong anticorrelation between the two quantities. This is confirmed using both a Spearman rank-order correlation test and Kendall's τ, both of which show the anticorrelation to be significant with >99.99 per cent confidence. The upper limits to the variance in the case where no variability is detected, which are shown in the upper panel of Fig. 2, are generally above the measured values (for a given mass). This means they are unlikely to affect significantly any model fitting and we ignore them in the analysis below.

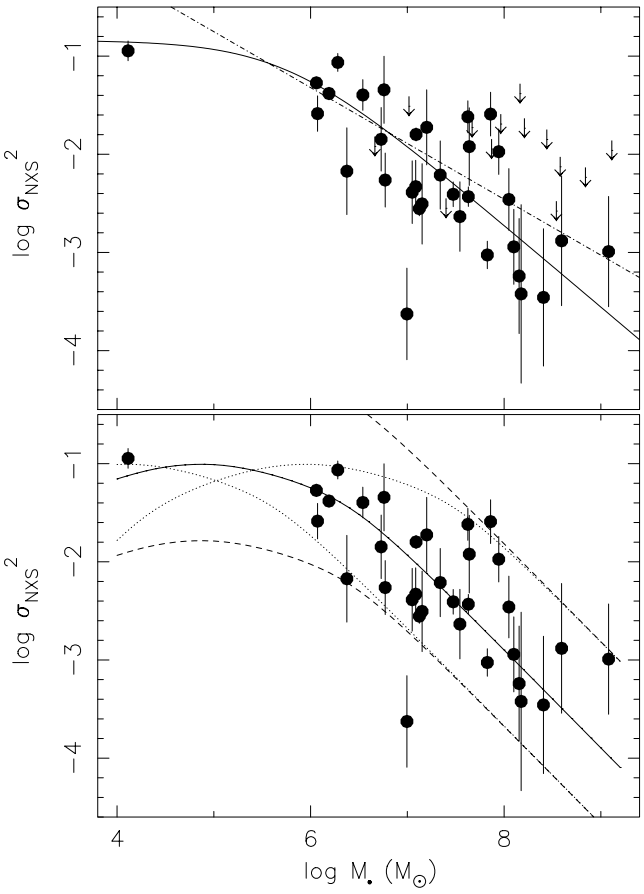

Figure 2. Log of excess variance versus log of black hole mass. In the top panel, the dot-dashed and solid lines show the best-fitting power law and bending power-law models, respectively. In the bottom panel, the solid line shows the best-fitting universal power spectrum model. The dotted and dashed lines illustrate the effect of varying either $C_{\rm HFB}$ or $\rm PSD_{AMP}$, respectively (see text for details). The $\sigma^2_{\rm NXS}$ upper limits are, for clarity, shown only in the upper panel.

While there is a strong general trend for objects with higher mass to be less variable, there is clearly substantial scatter in the variance–mass relationship. As we have, for the first time, presented realistic estimates of the uncertainties on $\sigma^2_{\rm NXS}$ we can be confident that this scatter is not owing only to these uncertainties.

There is also evidence from the plot – albeit based solely on the lowest mass object, NGC 4395 – that the variance–mass relationship is non-linear. This is expected in the presence of breaks in the power spectrum (e.g. Papadakis 2004), as we now show by modelling the variance–mass relationship using both simple parametrizations and with a specific power-spectral form.

4 MODELLING THE RELATIONSHIP BETWEEN EXCESS VARIANCE AND MASS

Having obtained the mean $\sigma^2_{\rm NXS}$ for each object, we then wished to model the relation between $\sigma^2_{\rm NXS}$ and $M_\bullet$. All fits were performed on $\log M_\bullet$ and $\log \sigma^2_{\rm NXS}$. We fitted the data using both a simple parametrization and also with a model that assumes the existence of a universal power spectrum.

4.1 Simple parametrizations

We initially modelled the data using a power law of the form $\sigma^2_{\rm NXS} = AM_\bullet{}^{-\gamma}$. The index and normalization of the best-fitting power law were $\gamma = 0.570$ and $A = 125$, respectively, and the reduced chi-squared was $\chi^2_\nu/{\rm DOF} = 8.05/31$. This model is shown as a dot-dashed line in the top panel of Fig. 2. We do not quote uncertainties in the best-fitting parameter values because the χ^2_ν is formally unsatisfactory.

We then used a singly broken bending power law defined as:

$$\sigma^2_{\rm NXS} = AM_\bullet{}^{-\gamma_{\rm low}} \left[1 + \left(\frac{M_\bullet}{M_{\bullet\rm bend}}\right)^{\gamma_{\rm high}-\gamma_{\rm low}}\right]^{-1} \quad (3)$$

where A is the normalization factor and the function bends from a power-law slope of $\gamma_{\rm low}$ to $\gamma_{\rm high}$ at the bend mass $M_{\bullet\rm bend}$.

We fixed the lower index to $\gamma_{\rm low} = 0$. The best-fitting bend mass, normalization and upper index were $M_{\bullet\rm bend} = 5.59 \times 10^5$ M$_\odot$, $A = 0.144$ and $\gamma_{\rm high} = 0.836$, respectively ($\chi^2_\nu/{\rm DOF} = 5.99/30$). The bending power law clearly improves the fit statistic substantially, but it is difficult to assess the formal improvement with, e.g. an F-test, as the fits are so poor.

4.2 Predicting $\sigma^2_{\rm NXS}$ from a power spectrum model

Based on recent power-spectral analyses of AGN, it is possible that the power spectra of AGN have the same shape with the time-scale of the variations being proportional to black hole mass (see the Introduction and references therein). We decided to investigate this possibility by modelling the relationship between $\sigma^2_{\rm NXS}$ and $M_\bullet$ with the assumption of a universal power spectrum. A model estimate can be made simply by integrating the continuous power spectrum over some frequency range, for example as defined by the length and the time bin size of the observation (e.g. Papadakis 2004). This, however, neglects the effects from the sampling pattern of the light curve, specifically the fact that it is binned, may have gaps, and is of finite

duration. For reasons discussed below these effects, particularly that of the finite duration and subsequent 'red-noise leak', are likely to be more important on the time-scales considered here than the much longer ones discussed by Papadakis (2004). We have taken an analytical approach to determining the model-predicted $\sigma^2_{\rm NXS}$, rather than use simulations as is typical for power-spectrum analysis (e.g. Uttley et al. 2002). Our approach is preferable for two reasons. First, simulations are far more computer-intensive, and second they rely on the simulation technique accurately reproducing the characteristics of the physical process giving rise to the variability. While the technique described below applies to calculation of model $\sigma^2_{\rm NXS}$ values it can be adapted straightforwardly to the estimation of discrete model power spectra.

According to Parseval's theorem, the variance in a binned light curve is equal to the sum of the powers in the observed *discrete* power spectrum of that light curve. The model power spectrum, however, is initially defined in a functional form and is thus *continuous*. We denote this continuous power spectrum as $P_{\rm M}(\nu)$. We need to determine how the discrete power spectrum $P_{\rm D}(\nu)$ is related to $P_{\rm M}(\nu)$. The following description is appropriate for evenly sampled light curves containing no gaps and having an even number of bins. Note also that the model power spectrum $P_{\rm M}(\nu)$ must be defined to be *two-sided* and, since we are dealing with a noise process, we refer to the expectation value of each power.

The first effect to consider is binning. Suppose we have a continuous process, with power spectrum $P_{\rm M}(\nu)$, and we transform it into a discrete process by binning the signal over a time period of δt. The power spectrum of the observed binned light curve, say $P_{\rm B}(\nu)$, is related to $P_{\rm M}(\nu)$ through the following relation:

$$\langle P_{\rm B}(\nu)\rangle = B(\nu)P_{\rm M}(\nu) \tag{4}$$

where the binning function $B(\nu)$ (van der Klis 1989) is given by

$$B(\nu) = \left[\frac{\sin(\pi\nu\delta t)}{\pi\nu\delta t}\right]^2. \tag{5}$$

The next effect to consider is aliasing. The fact that the observed light curve is sampled at discrete intervals means that power can leak into the power spectrum from above the Nyquist frequency $\nu_{\rm Nyq} = 1/(2\delta t)$. The binned and aliased power spectrum, say $P_{\rm BA}(\nu)$, is related to the intrinsic power spectrum, $P_{\rm M}(\nu)$, through the relation (Priestley 1989)

$$\langle P_{\rm BA}(\nu)\rangle = \sum_{i=-\infty}^{\infty}\langle P_{\rm B}(\nu + i/\delta t)\rangle. \tag{6}$$

The power in one of our typical model power spectra decreases sharply with frequency and the data are binned. This means that only a relatively small amount of power is aliased into the observed frequency range. Accordingly, we found that summing from $i = -10$ to $i = 10$ was easily sufficient to account for aliasing. Power spectra that are either flat or increase with frequency might require a larger range in i.

The final effect to account for is red-noise leak. This occurs when variations exist at frequencies lower than those sampled by the observed light curve, as is the case for a red-noise process. This 'leakage' of power from low to high frequencies can be seen as either a rising or falling trend over the duration of the light curve. The power spectrum of the final light curve, i.e. $P_{\rm D}(\nu)$, is related to the intrinsic power spectrum, i.e. $P_{\rm M}(\nu)$, by the convolution of the $\langle P_{\rm BA}(\nu)\rangle$ with the so-called 'window function' $W(\nu)$ of the observed light curve. For evenly sampled light curves, $W(\nu)$ is simply Fejer's kernel (e.g. Priestley 1989):

$$W(\nu) = \frac{1}{T}\left[\frac{\sin(\pi\nu T)}{\pi\nu}\right]^2 \tag{7}$$

where T is the duration of the light curve. We performed the convolution with the numerical integral:

$$P_{\rm D}(\nu) = 2\sum_{i=-Nf/2}^{Nf/2}\langle P_{\rm BA}(i\delta\nu')\rangle W(\nu - i\delta\nu')\delta\nu' \qquad (\nu = 1/T, 2/T, \ldots, \nu_{\rm Nyq}). \tag{8}$$

In the above sum, N is the number of bins in the light curve and f is a positive integer. The frequency step $\delta\nu'$ is given by $\delta\nu' = 1/(Tf)$. The value of f must be large enough so that the convolution extends to a low enough frequency to account for all of the low-frequency power. Determining a suitable value of f required a process of trial and error. We performed the convolution with successively higher values of f until further increases produced only a negligible effect. We found that $f = 500$ was sufficient for all our convolutions. Note that the introduction of the factor 2 in equation (8) means that $P_{\rm D}(\nu)$ is *single-sided* and it is defined only for $N/2$ frequencies. Also note that, for $i\delta\nu' = \pm\nu_{\rm Nyq}$, the term $\delta\nu'$ was replaced by $\delta\nu'/2$, to account for the end effects in the numerical integral.

The expected excess variance was then determined by summing the powers in $P_{\rm D}(\nu)$:

$$\sigma^2_{\rm NXS,model} = \left[\sum_{i=1}^{N/2-1} P_{\rm D}(i/T)\delta\nu\right] + \frac{1}{2}P_{\rm D}(\nu_{\rm Nyq})\delta\nu \tag{9}$$

where $\delta\nu = 1/T$. The factor of $1/2$ is required for $P_{\rm D}(\nu_{\rm Nyq})$ because in a double-sided power spectrum the Nyquist frequency occurs only once. The factor $\delta\nu$ is required because the power is expressed in units of fractional rms-squared per Hz.

Each of our 305 light-curve segments has its own particular duration and sampling pattern, and there are many gaps in the data train. Therefore, the window function will be different for each segment and will not, in general, be represented by Fejer's kernel. However, the presence of missing bins in the light curve will affect only the scatter in the $\sigma^2_{\rm NXS}$ measurements, with the mean value being unaffected. Moreover, we have taken care to use light-curve segments of similar durations. Therefore, we were able to simplify the modelling procedure by assuming that our light curves were all fully sampled with the same number of bins. We used $N = 148$, as this is the even number-of-bins closest to the mean segment duration of 38 143.5 s. Having made this simplification, we were required to determine only a single value of $\sigma^2_{\rm NXS,model}$ for each object (for a certain model power spectrum), thus speeding up the modelling process.

4.3 A universal power spectrum model

Motivated by power-spectral analyses of AGN (see the Introduction, and in particular Markowitz et al. 2003), and following the recent work of Papadakis (2004), we hypothesized a universal power spectrum of the form:

$$P_{\rm M}(\nu) = A(\nu_{\rm LFB}/\nu_{\rm HFB})^{-1}(\nu \leqslant \nu_{\rm LFB}) \tag{10}$$

$$P_{\rm M}(\nu) = A(\nu/\nu_{\rm HFB})^{-1}(\nu_{\rm LFB} < \nu < \nu_{\rm HFB}) \tag{11}$$

$$P_{\rm M}(\nu) = A(\nu/\nu_{\rm HFB})^{-2}(\nu_{\rm HFB} \leqslant \nu) \tag{12}$$

where the normalization factor A is the power at the high-frequency break $\nu_{\rm HFB}$. The value of $\nu_{\rm HFB}$ is assumed to decrease with black hole mass, according to the expression $\nu_{\rm HFB} = C_{\rm HFB}/M_\bullet$, where $C_{\rm HFB}$

Table 2. Best-fitting values for fits using the universal power spectrum model.

Excluded objects	$C_{\rm HFB}$ (Hz $M_\odot$)	$\rm PSD_{AMP}$	χ^2_ν/DOF
(1)	(2)	(3)	(4)
None (all objects are included)	43	0.024	6.24/31
NGC 4395	53	0.021	6.30/30
AKN 564, MCG−6-30-15, TON S180, NGC 4151, NGC 3516, NGC 5548	55	0.033	4.30/24

(1) Objects excluded from fit. (2) Scaling constant for the high-frequency break $\nu_{\rm HFB}$, where $\nu_{\rm HFB} = C_{\rm HFB}/M_\bullet$. (3) Power-spectral amplitude at $\nu_{\rm HFB}$ in power × frequency space. (4) Reduced chi-squared and degrees of freedom for fit.

is a constant and $M_\bullet$ is the mass of the black hole in units of $\rm M_\odot$. The low-frequency break is related to the high-frequency break by $\nu_{\rm LFB} = \nu_{\rm HFB}/C_{\rm LFB}$ where $C_{\rm LFB}$ is a constant. The normalization A varies as a function of $\nu_{\rm HFB}$ as $A = \rm PSD_{AMP}/\nu_{HFB}$, where $\rm PSD_{AMP}$ is assumed to be the same for all objects. Using this model, the relation between variance and mass can therefore be described with three parameters: $C_{\rm HFB}$, $C_{\rm LFB}$ and $\rm PSD_{AMP}$.

To determine the best-fitting model, we minimized χ^2 for grid of values of $C_{\rm HFB}$, $C_{\rm LFB}$ and $\rm PSD_{AMP}$ values. We found that we could not constrain the parameter $C_{\rm LFB}$. This is because the low-frequency break generally does not fall within our sampled frequency range. Therefore, we fixed this at $C_{\rm LFB} = 20$. This is roughly the value of $C_{\rm LFB}$ observed in the AGN NGC 3783 (Markowitz et al. 2003) and in Cyg X-1 in the low/hard state (Belloni & Hasinger 1990a; Nowak et al. 1999).

The best-fitting values of $C_{\rm HFB}$ and $\rm PSD_{AMP}$ are given in Table 2. This best-fitting model (for the fit including all 33 objects) is shown as the solid line in Fig. 2 (bottom). The probability of exceeding the χ^2_ν of the best-fitting universal model is 2×10^{-25}. This indicates that, while the model appears to describe rather well the overall trend of decreasing $\sigma^2_{\rm NXS}$, there exists significant scatter not accounted for by the model. The residuals $\Delta\log\sigma^2_{\rm NXS}$ from this model are listed in Table 1. We also fitted the universal model to the data excluding various objects. As seen in Table 2, neither the lowest mass object (viz. NGC 4395), nor the six objects with the largest number of light-curve segments (viz. AKN 564, MCG−6-30-15, TON S180, NGC 4151, 3516, 5548), dominate the fit.

The scatter present in the relationship between $\log\sigma^2_{\rm NXS}$ and $\log M_\bullet$ can be explained with a variation of either $C_{\rm HFB}$ or $\rm PSD_{AMP}$ from their best-fitting values. This is illustrated in Fig. 2 (bottom). We find that a range in $C_{\rm HFB}$ values between 7.2 and 520 (upper and lower dotted-lines, respectively), or a range in $\rm PSD_{AMP}$ between 0.004 and 0.29 (upper and lower dashed lines, respectively), can account for most of the scatter in the $\log\sigma^2_{\rm NXS}$ versus $\log M_\bullet$ relation.

The scatter might also be owing to a combination of the uncertainties in $\log\sigma^2_{\rm NXS}$ *and* $\log M_\bullet$, the latter of which are typically about 0.5 dex (e.g. Woo & Urry 2002; Peterson et al. 2004). We performed simulations to investigate this possibility, adopting the best-fitting relation between $\log\sigma^2_{\rm NXS}$ and $\log M_\bullet$ as our model. We needed first to obtain a set of 33 model data points to which we could then apply scatter in $\log\sigma^2_{\rm NXS}$ and $\log M_\bullet$. To do this, we projected each of our 33 observed data points on to the best-fitting relation, minimizing the distance between the observed point and the model. (The distance between an observed data point and any particular location on the model relation was calculated from the differences in $\log\sigma^2_{\rm NXS}$ and $\log M_\bullet$ between the observed point and the model, divided by the corresponding uncertainty in the observed values.) Having thus adopted a set of 33 model data points, we then performed 1000 simulations. Each of these involved adding scatter to the model points and then determining the χ^2_ν between the simulated data points and the model relation. We found that 79 per cent of the simulations produced a χ^2_ν exceeding that found for the observed data. Therefore, the scatter that we have observed in the relation between $\log\sigma^2_{\rm NXS}$ and $\log M_\bullet$ might be owing only to measurement uncertainties. If this is indeed the case, then we would expect this scatter to be unrelated to other properties of the objects in our sample, and we investigate this possibility in the following section.

5 THE ORIGIN OF THE SCATTER IN THE VARIANCE–MASS RELATIONSHIP

Previous studies have revealed an anticorrelation between $\sigma^2_{\rm NXS}$ and X-ray luminosity, and a positive correlation between $\sigma^2_{\rm NXS}$ and photon index Γ (e.g. Nandra et al. 1997a; Turner et al. 1999; Markowitz & Edelson 2001; Papadakis 2004). Given the strong dependence between the $\sigma^2_{\rm NXS}$ and $M_\bullet$, it is of interest to see whether these correlations still exist when this primary dependence is removed. This should allow us to shed light on the origin of the scatter in the variance–mass relationship.

In Fig. 3 we plot $\log\sigma^2_{\rm NXS}$, $\log M_\bullet\ \sigma^2_{\rm NXS}$, and the residuals $\Delta\log\sigma^2_{\rm NXS}$ from the best-fitting universal model, versus the

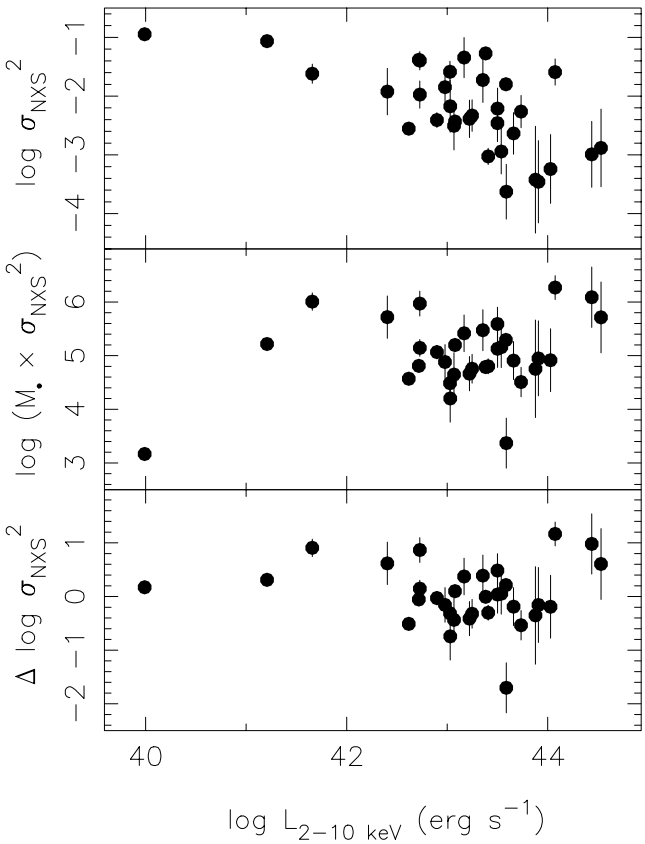

Figure 3. Log of excess variance (top), log of the product of excess variance and black hole mass (middle), and excess variance residuals (bottom), versus log of the 2–10 keV luminosity.

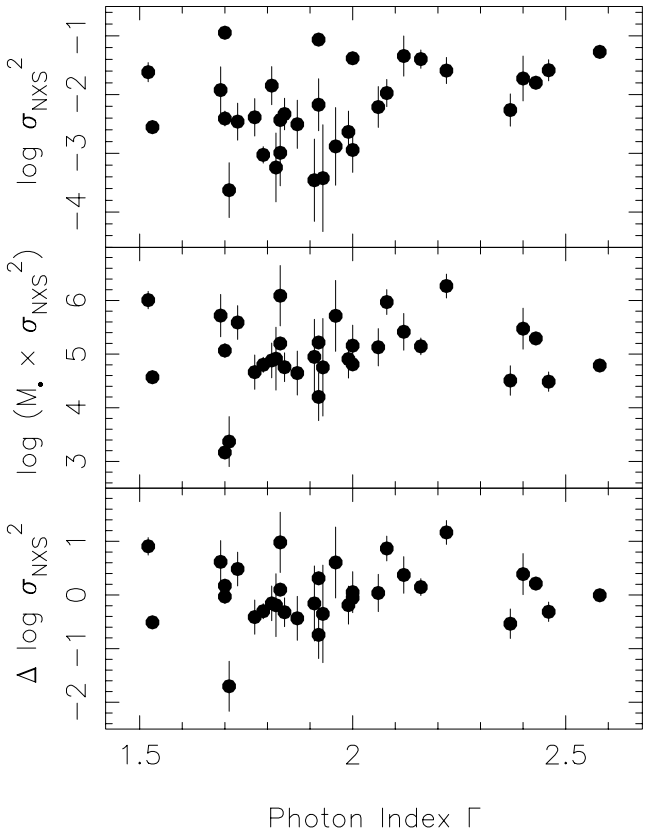

Figure 4. Log of excess variance (top), log of the product of excess variance and black hole mass (middle), and excess variance residuals (bottom), versus the 2–10 keV photon index.

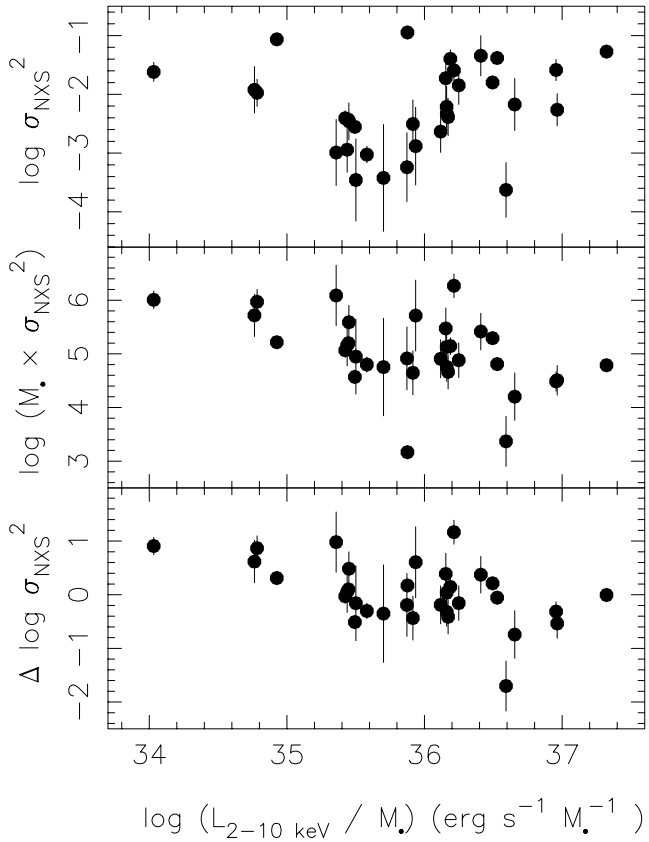

Figure 5. Log of excess variance (top), log of the product of excess variance and black hole mass (middle), and excess variance residuals (bottom), versus log of the 2–10 keV luminosity normalized by the black hole mass.

logarithm of the 2–10 keV luminosity. The quantities $\log M_\bullet\,\sigma^2_{\rm NXS}$ and $\Delta\log\sigma^2_{\rm NXS}$ are useful because they remove the mass dependence. Note that the quantity $\log M_\bullet\,\sigma^2_{\rm NXS}$ is model-independent. In Figs 4 and 5 we plot the variability parameters versus, respectively, the photon index and the logarithm of the 2–10 keV luminosity normalized to the black hole mass, $\log(L_{2\text{–}10\,\rm keV}/M_\bullet)$. To the extent that the X-ray luminosity is proportional to the bolometric luminosity, as is commonly assumed, the value $\log(L_{2\text{–}10\,\rm keV}/M_\bullet)$ is proportional to the ratio between the mass-accretion rate and that required to reach the Eddington luminosity (i.e. the 'Eddington ratio'). Note that the correction factor between the 2–10 keV and bolometric luminosities is uncertain, with considerable scatter. The Spearman rank-order correlation coefficient and Kendall's τ of all nine relationships are presented in Table 3.

As with previous studies, we find a very strong correlation between $\log\sigma^2_{\rm NXS}$ and $\log L_{2\text{–}10\,\rm keV}$ (see Fig. 3). This correlation disappears when we remove the dependence of $\sigma^2_{\rm NXS}$ on $M_\bullet$. It seems most likely that the primary correlation is in fact with mass, and that the apparent correlation with $\log L_{2\text{–}10\,\rm keV}$ is secondary.

A similar situation is present when considering the photon index (see Fig. 4). Indeed, the correlation between $\log\sigma^2_{\rm NXS}$ and Γ is not very strong in any event, being significant at only the 96 per cent confidence level, though there does seem to be an absence of objects having both a steep photon index and low $\sigma^2_{\rm NXS}$. When the mass dependence is accounted for, however, no residual correlation remains. In the plot of $\Delta\log\sigma^2_{\rm NXS}$ versus Γ, the steep-spectrum objects do not have a systematically higher $\Delta\log\sigma^2_{\rm NXS}$ than the others.

Finally, we consider the relationship between the variability properties and the normalized luminosity $\log(L_{2\text{–}10\,\rm keV}/M_\bullet)$ (see Fig. 5). There is considerable scatter, and no strong correlation, between $\log\sigma^2_{\rm NXS}$ and $\log(L_{2\text{–}10\,\rm keV}/M_\bullet)$. Here, however, we do find a significant relationship between $\log(L_{2\text{–}10\,\rm keV}/M_\bullet)$ and both the mass-normalized excess variance and the residuals from our best-fitting model. The latter correlation is significant with ∼99 per cent confidence and, perhaps surprisingly, it is in the sense that objects with larger values of normalized luminosity are *less* variable for a given mass. While significant, this relationship should be treated with some caution. The presence of random scatter in the black hole mass estimates could possibly induce such an anticorrelation. If $M_\bullet$ is underestimated then $\Delta\log\sigma^2_{\rm NXS}$ will also be underestimated and $\log(L_{2\text{–}10\,\rm keV}/M_\bullet)$ will be overestimated. An artificial anticorrelation would certainly be induced if all objects had the same value of $\log(L_{2\text{–}10\,\rm keV}/M_\bullet)$. However, it is less clear that this effect could produce an anticorrelation between $\Delta\log\sigma^2_{\rm NXS}$ and $\log(L_{2\text{–}10\,\rm keV}/M_\bullet)$ in our data because the normalized luminosities in our sample span three orders of magnitude. We used the simulations described in Section 4.3 to test whether the observed anticorrelation could be owing to the uncertainties in the black hole masses. For each of the 1000 simulations, we calculated $\log\sigma^2_{\rm NXS}$ and $\log(L_{2\text{–}10\,\rm keV}/M_\bullet)$ from the simulated data points and measured Kendall's τ. We found that, even with no intrinsic anticorrelation between $\sigma^2_{\rm NXS}$ and $L_{2\text{–}10\,\rm keV}/M_\bullet$, 57 per cent of the simulations gave a Kendall's τ that was *more negative* than the observed value of −0.31. Therefore, we cannot rule out the possibility that the observed anticorrelation between $\Delta\log\sigma^2_{\rm NXS}$ and $\log(L_{2\text{–}10\,\rm keV}/M_\bullet)$ is an artefact induced by the presence of uncertainties in the measurements of black hole mass.

Table 3. Correlation coefficients between X-ray variability properties and the 2–10 keV luminosity, photon index and normalized luminosity.

Observables		Spearman		Kendall	
		Coeff.	Sig. (per cent)	Coeff.	Sig. (per cent)
(1)	(2)	(3)	(4)	(5)	(6)
$\log L_{2-10\,\mathrm{keV}}$	$\log \sigma^2_{\mathrm{NXS}}$	−0.61	99.98	−0.43	99.96
	$\log M_\bullet\, \sigma^2_{\mathrm{NXS}}$	0.13	53	0.10	59
	$\Delta\log \sigma^2_{\mathrm{NXS}}$	−0.06	25	−0.04	26
Γ	$\log \sigma^2_{\mathrm{NXS}}$	0.36	96	0.25	96
	$\log M_\bullet\, \sigma^2_{\mathrm{NXS}}$	0.10	43	0.10	56
	$\Delta\log \sigma^2_{\mathrm{NXS}}$	0.11	44	0.09	53
$\log (L_{2-10\,\mathrm{keV}}/M_\bullet)$	$\log \sigma^2_{\mathrm{NXS}}$	0.29	89	0.19	89
	$\log M_\bullet\, \sigma^2_{\mathrm{NXS}}$	−0.50	99.7	−0.36	99.7
	$\Delta\log \sigma^2_{\mathrm{NXS}}$	−0.44	99.0	−0.31	98.8

(1) X-ray spectral property on the abscissa. (2) X-ray variability property on the ordinate. (3) Spearman rank-order correlation coefficient. (4) Significance of correlation. (5) Kendall's τ. (6) Significance of correlation.

6 DISCUSSION

6.1 Summary of results

We have investigated the relationship between normalized excess variance and black hole mass for a sample of 46 radio-quiet AGN. We restricted our light curves to have durations between ∼30 and 40 ks (rest-frame), allowing us to probe nearly the same range of time-scales for all objects. There were 32 objects in our sample that had more than one light-curve segment. For these objects, we were able to determine the mean σ^2_{NXS}, decreasing the uncertainty in the measurements. Moreover, for six objects, there were more than 15 light-curve segments available. An examination of the distributions of the individual σ^2_{NXS} values for these six objects allowed us to estimate the uncertainties in the mean σ^2_{NXS} for every object in our sample. These uncertainties incorporate the effects of both measurement uncertainties and the stochastic nature of the variability. Of the 46 objects in our sample, 33 were found to be variable. As with previous studies using *ASCA* (Lu & Yu 2001; Bian & Zhao 2003; Markowitz & Edelson 2004) and *RXTE* (Markowitz & Edelson 2004; Papadakis 2004) data, we found a significant anticorrelation between σ^2_{NXS} and $M_\bullet$.

We initially fitted the relationship between σ^2_{NXS} and $M_\bullet$ with both a power law and bending power law. Neither of these fits were formally satisfactory; however, the bending power law was an improvement over the unbroken power law.

We also fitted the data with a universal power-spectrum model. We determined the expected σ^2_{NXS} from the model as a function of $M_\bullet$, accounting for the effects of binning, aliasing, and red-noise leak in the observed light curves. The best-fitting high-frequency break × mass scaling coefficient was $C_{\mathrm{HFB}} = 43$ Hz $\mathrm{M}_\odot$, and the best-fitting amplitude was $\mathrm{PSD}_{\mathrm{AMP}} = 0.024$. In his study using *RXTE* data, Papadakis (2004) found values of $C_{\mathrm{HFB}} = 17$ and $\mathrm{PSD}_{\mathrm{AMP}} = 0.017$ ($C_{\mathrm{HFB}} = 340$ for NGC 4051). Markowitz & Edelson (2004) studied the variability of Seyfert 1 galaxies on various time-scales and found that, on average, the variability time-scale followed the relation $T_{\mathrm{b}} = M_\bullet/10^{6.7}$ d. Using our parametrization, this corresponds to a scaling factor of $C_{\mathrm{HFB}} = 58$ Hz $\mathrm{M}_\odot$.

In general, the mass–variance anticorrelation can therefore be understood very simply by assuming that all size-scales scale with mass, and hence so do all characteristic time-scales (such as those represented by the break frequencies). Our analysis furthermore supports the idea that the average, or typical power spectrum of AGN resembles the 'universal' power spectrum discussed above. The best-fitting universal model was not satisfactory, however, with $\chi^2_\nu/\mathrm{DOF} = 6.30/31$, indicating that, for a certain $M_\bullet$, there exists significant scatter in the σ^2_{NXS} values. However, our simulations showed that uncertainties in the mass measurements can account for this scatter.

6.2 The origin of scatter in the variance–mass relation

Previous work has suggested that the excess variance is related to source properties other than mass, such as the luminosity, X-ray spectral index and Hβ linewidth (e.g. Nandra et al. 1997a; Turner et al. 1999). We have reinvestigated some of these relations here. Consistent with previous work using *ASCA* data, we found a correlation between $\log \sigma^2_{\mathrm{NXS}}$ and $\log L_{2-10\,\mathrm{keV}}$ (e.g. Nandra et al. 1997a; Leighly 1999a; Turner et al. 1999). The fact that no correlation exists when the dependence of σ^2_{NXS} on $M_\bullet$ is removed suggests that the correlation between $\log \sigma^2_{\mathrm{NXS}}$ and $\log L_{2-10\,\mathrm{keV}}$ is largely a result of the $\sigma^2_{\mathrm{NXS}} - M_\bullet$ relation. This effect has also been seen in *RXTE* data with a time-scale of about 300 d (Papadakis 2004).

We also found an absence of objects having both a steep photon index and low σ^2_{NXS}. After accounting for the dependence on mass, however, we found no evidence for a correlation between excess variance and X-ray spectral index. This is perhaps surprising, as previous work has suggested that narrow-line Seyfert 1 galaxies – which have soft X-ray spectra as a general characteristic (e.g. Boller, Brandt & Fink 1996; Brandt, Mathur & Elvis 1997) – are more

variable than their broad-line analogues (Leighly 1999a; Turner et al. 1999). An effect similar to that which we have observed has already been noted by other workers using *ASCA* data. Lu & Yu (2001) found that the narrow-line Seyfert 1 galaxies in their sample appeared to follow the same variance–mass relation as the broad-line objects. Bian & Zhao (2003), in an expanded study using the variance measurements of Turner et al. (1999) and Lu & Yu (2001), also found that the AGN with FWHM(Hβ) less than 2000 km s^{-1} appeared to follow the same relation as those objects with broad Hβ emission lines (see also the discussion in Markowitz & Edelson 2004).

We also found an anticorrelation between excess variance residuals and the normalized luminosity ($L_{2\text{–}10\,\mathrm{keV}}/M_\bullet$), which we shall now simply refer to as the Eddington ratio $\dot{M}$. Our simulations showed that this apparent anticorrelation between $\Delta\log\sigma^2_{\mathrm{NXS}}$ and $\dot{M}$ could be an artefact owing to the uncertainties in the measurements of the black hole masses. The fact that we did not find a *positive* correlation between excess variance and $\dot{M}$, *for a given mass*, is surprising: in the prevailing paradigm, NLS1s generally show more variability and are thought also to be accreting at high Eddington ratios (Pounds, Done & Osborne 1995). It is not yet clear, then, that a high value of $\dot{M}$ is a contributing factor to an AGN exhibiting a relatively large excess variance. Further investigations in this regard will benefit enormously from future improvements in black hole mass measurements.

6.3 Models for X-ray variability

In the standard coronal model, which can be applied both to stellar-mass black holes and AGN, seed photons from an optically thick accretion disc are inverse Compton scattered by hot electrons in an accretion disc corona (e.g. Sunyaev & Titarchuk 1980; Haardt & Maraschi 1993; Churazov, Gilfanov & Revnivtsev 2001; McClintock & Remillard 2005).

One class of models involves the superposition of individual 'shots' in the light curve (Terrell 1972). These shots are possibly associated with magnetic flares in the corona (e.g. Poutanen & Fabian 1999, and references therein). In the model of Poutanen & Fabian (1999), there is a distribution of shot time-scales, with the value of ν_{HFB} being inversely proportional to the duration of the longest shots. Also in that model, the variance of the counting-rate fluctuations is inversely proportional to the mean rate λ of the occurrence of flares. One can then assume a basic framework in which all size-scales (and, therefore, time-scales) and the luminosity of the individual shots is proportional to the black hole mass, accounting for the main variance–mass relationship. The total luminosity is proportional to λ, so for a given black hole mass the variance in the light curve is expected to be inversely proportional to the Eddington ratio.

In the so-called 'propagating perturbation' class of models, variations in the accretion rate occur over a range of radii from the black hole (e.g. Lyubarskii 1997; Churazov et al. 2001; Kotov, Churazov & Gilfanov 2001; Uttley 2004, and references therein). Slower variations occur at larger radii and propagate inwards, coupling together with the faster variations produced at smaller radii. The modulations in the accretion rate propagate to the X-ray emission region and produce variations in the X-ray flux. This type of model is attractive because it can provide an explanation for the well-known 'rms–flux' relation seen in X-ray binaries and AGN (e.g. Uttley & McHardy 2001; Gaskell 2004; Uttley 2004). The value of ν_{HFB} is expected to be inversely proportional to the size of the X-ray emission region because the variations that originate from within the emission region are suppressed (Churazov et al. 2001; Uttley 2004). In the model of Churazov et al. (2001), the low/hard state in Cyg X-1 occurs when the optically thick, geometrically thin accretion disc is truncated far from the emission region. In the high/soft state, the disc reaches all the way down to the emission region and this leads to the X-ray variations following an unbroken $\alpha = 1$ power law. In this model, it is not fully specified how the emission region changes as the inner radius of the disc varies. It is clear, however, that the emission region would need to become smaller as the disc approaches that region because ν_{HFB} is higher in the high/soft state than in the low/hard state.

McHardy et al. (2004) appealed to the analogy with black hole X-ray binaries and speculated that the location of the inner edge of the accretion disc in AGN is perhaps related to the mass-accretion rate or the black hole spin. For a certain black hole mass, then, different AGN might be regarded as existing in different states, just as Cyg X-1 is observed in different states. In this scenario, we would expect the X-ray variability of AGN to be related not only to the black hole mass but also the Eddington ratio and photon index. Objects having a relatively high $\dot{M}$ and soft X-ray spectra would, for a certain value of $M_\bullet$, have a relatively high value of ν_{HFB} (i.e. a high value of C_{HFB}) and should, therefore, exhibit a relatively high value of σ^2_{NXS} for a given range in time-scales. We found no evidence that the X-ray variability depends on these properties, and so the reality of this scenario remains to be established. Note, however, that if an anticorrelation existed between C_{HFB} and $\mathrm{PSD}_{\mathrm{AMP}}$, then C_{HFB} could possibly increase without there being a corresponding increase in σ^2_{NXS}.

Discriminating between various possible scenarios obviously requires the use of power-spectral analyses, preferably covering a wide range in source properties. The challenge, then, is to assemble enough high-quality power spectra so that we can relate the power-spectral parameters not only to $M_\bullet$ but also to the Eddington ratio and other quantities such as photon index. We note, in particular, that an analysis of the AGN data in the *XMM–Newton* and *Chandra* archives, even from relatively short observations, would be useful in studying the properties (e.g. power-law slopes) of the variability at frequencies above the high-frequency break. A natural starting point, of course, is to conduct a rigorous comparison between the currently available power spectra (e.g. Uttley et al. 2002; Markowitz et al. 2003; McHardy et al. 2004) and the other relevant source properties. Any conclusions drawn from these comparisons could then be tested on a larger sample of objects by using measurements of excess variance.

ACKNOWLEDGMENTS

The authors are grateful to Brad Peterson for kindly providing some black hole mass measurements prior to publication. We also thank the anonymous referee for helpful suggestions and comments. This research has made use of the Tartarus (Version 3.0) database, created by Paul O'Neill and Kirpal Nandra at Imperial College London, and Jane Turner at NASA/GSFC. Tartarus is supported by funding from PPARC, and NASA grants NAG5-7385 and NAG5-7067. PMO acknowledges financial support from PPARC.

REFERENCES

Belloni T., Hasinger G., 1990a, A&A, 230, 103
Belloni T., Hasinger G., 1990b, A&A, 227, L33
Bian W., Zhao Y., 2003, MNRAS, 343, 164
Blanco P. R., Ward M. J., Wright G. S., 1990, MNRAS, 242, 4P
Boller T., Brandt W. N., Fink H., 1996, A&A, 305, 53

Brandt W. N., Mathur S., Elvis M., 1997, MNRAS, 285, L25
Churazov E., Gilfanov M., Revnivtsev M., 2001, MNRAS, 321, 759
Cui W., Heindl W. A., Rothschild R. E., Zhang S. N., Jahoda K., Focke W., 1997, ApJ, 474, L57
Edelson R., Nandra K., 1999, ApJ, 514, 682
Edelson R., Turner T. J., Pounds K., Vaughan S., Markowitz A., Marshall H., Dobbie P., Warwick R., 2002, ApJ, 568, 610
Filippenko A. V., Ho L. C., 2003, ApJ, 588, L13
Gaskell C. M., 2004, ApJ, 612, L21
Gebhardt K. et al., 2000, ApJ, 539, L13
George I. M., Turner T. J., Yaqoob T., Netzer H., Laor A., Mushotzky R. F., Nandra K., Takahashi T., 2000, ApJ, 531, 52
Green A. R., McHardy I. M., Lehto H. J., 1993, MNRAS, 265, 664
Grupe D., Wills B. J., Leighly K. M., Meusinger H., 2004, AJ, 127, 156
Haardt F., Maraschi L., 1993, ApJ, 413, 507
Iwasawa K., Fabian A. C., Almaini O., Lira P., Lawrence A., Hayashida K., Inoue H., 2000, MNRAS, 318, 879
Kaspi S., Smith P. S., Netzer H., Maoz D., Jannuzi B. T., Giveon U., 2000, ApJ, 533, 631
Kotov O., Churazov E., Gilfanov M., 2001, MNRAS, 327, 799
Lawrence A., Papadakis I., 1993, ApJ, 414, L85
Leighly K. M., 1999a, ApJS, 125, 297
Leighly K. M., 1999b, ApJS, 125, 317
Lu Y., Yu Q., 2001, MNRAS, 324, 653
Lyubarskii Y. E., 1997, MNRAS, 292, 679
Markowitz A., Edelson R., 2001, ApJ, 547, 684
Markowitz A., Edelson R., 2004, ApJ, 617, 939
Markowitz A. et al., 2003, ApJ, 593, 96
Marshall N., Warwick R. S., Pounds K. A., 1981, MNRAS, 194, 987
Marshall K., Ferrara E. C., Miller H. R., Marscher A. P., Madejski G., 2004, in Kaaret P., Lamb F. K., Swank J. H., eds, X-ray Timing 2003: Rossi and Beyond. American Institute of Physics, Melville, New York, pp. 182–185
McClintock J. E., Remillard R. A., 2005, in Lewin W. H. G., van der Klis M., eds, Compact Stellar X-ray Sources. Cambridge Univ. Press, Cambridge, in press
McHardy I., 1988, Mem. It. Astr. Soc, 59, 239
McHardy I. M., Papadakis I. E., Uttley P., Page M. J., Mason K. O., 2004, MNRAS, 348, 783
Nandra K., Papadakis I., 2001, ApJ, 554, 710
Nandra K., Pounds K. A., 1994, MNRAS, 268, 405
Nandra K., George I. M., Mushotzky R. F., Turner T. J., Yaqoob T., 1997a, ApJ, 476, 70
Nandra K., George I. M., Mushotzky R. F., Turner T. J., Yaqoob T., 1997b, ApJ, 477, 602
Nowak M. A., Vaughan B. A., Wilms J., Dove J. B., Begelman M. C., 1999, ApJ, 510, 874
Papadakis I. E., 2004, MNRAS, 348, 207
Papadakis I. E., Lawrence A., 1993, MNRAS, 261, 612
Papadakis I. E., McHardy I. M., 1995, MNRAS, 273, 923
Papadakis I. E., Brinkmann W., Negoro H., Gliozii M., 2002, A&A, 382, L1
Peterson B. M. et al., 2004, ApJ, 613, 682
Pounds K. A., Done C., Osborne J. P., 1995, MNRAS, 277, L5
Poutanen J., Fabian A. C., 1999, MNRAS, 306, L31
Press W. H., Teukolsky S. A., Vetterling W. T., Flannery B. P., 2001, Numerical Recipes in Fortran 77: The Art of Scientific Computing. Cambridge Univ. Press, Cambridge
Priestley M. B., 1989, Spectral Analysis and Time Series. Academic Press, London
Reeves J. N., Turner M. J. L., 2000, MNRAS, 316, 234
Revnivtsev M., Gilfanov M., Churazov E., 2000, A&A, 363, 1013
Reynolds C. S., 1997, MNRAS, 286, 513
Sunyaev R., Titarchuk L. G., 1980, A&A, 86, 121
Terrell N. J. J., 1972, ApJ, 174, L35
Turner T. J., George I. M., Nandra K., Turcan D., 1999, ApJ, 524, 667
Turner T. J., Nandra K., Turcan D., George I. M., 2001, in White N. E., Malaguti G., Palumbo G. G. C., eds, X-ray Astronomy: Stellar Endpoints, AGN, and the Diffuse X-ray Background. American Institute of Physics, Melville, New York, pp. 991–994
Uttley P., 2004, MNRAS, 347, L61
Uttley P., McHardy I. M., 2001, MNRAS, 323, L26
Uttley P., McHardy I. M., Papadakis I. E., 2002, MNRAS, 332, 231
van der Klis M., 1989, in Ögelman H., van den Heuvel E. P. J., eds, Timing Neutron Stars. Kluwer, Dordrecht, pp. 27–69
Vaughan S., Fabian A. C., 2003, MNRAS, 341, 496
Vaughan S., Edelson R., Warwick R. S., Uttley P., 2003a, MNRAS, 345, 1271
Vaughan S., Fabian A. C., Nandra K., 2003b, MNRAS, 339, 1237
Vaughan S., Iwasawa K., Fabian A. C., Hayashida K., 2005, MNRAS, 356, 524
Wandel A., Peterson B. M., Malkan M. A., 1999, ApJ, 526, 579
Wang T., Lu Y., 2001, A&A, 377, 52
Woo J. H., Urry C. M., 2002, ApJ, 579, 530

This paper has been typeset from a TEX/LATEX file prepared by the author.